IEEE Access
Multidisciplinary | Rapid Review | Open Access Journal

Received January 1, 2022, accepted January 25, 2022, date of publication February 7, 2022, date of current version February 11, 2022.

Digital Object Identifier 10.1109/ACCESS.2022.3148165

An Artificial Lateral Line Sensor Using Polyvinylidene Fluoride (PVDF) Membrane for Oscillatory Flow Sensing

TAN SHIZHE AND WANG YIJIN

Department of Electronic Engineering, Ocean University of China, Qingdao 266100, China

Corresponding author: Tan Shizhe (tanshizhe@ouc.edu.cn)

This work was supported by the Basic Scientific Research of the China Ministry of Education under Grant 201562008.

ABSTRACT Flow sensing is an essential technology used in marine science. Fish live in fluid environments. Therefore, it is not surprising that fish have developed abilities to sense flow. We designed an artificial lateral line sensor for oscillatory flow sensing by mimicking the lateral line organ of a fish. This sensor is composed of an artificial cupula that mimics the cupula of neuromasts, cantilever beam that mimics hair-like cilia, and perception unit that mimics hair cells. We designed four different cupula shapes and discussed the influence of the artificial cupula shape on the sensing performance. We analyzed the structure of the cantilever beam to determine its length. The perception unit uses a polyvinylidene fluoride (PVDF) membrane as the piezoelectric sensing element. To protect the sensor from harsh fluid environments, a well-designed waterproofing scheme was proposed. Finally, a dipole stimulus was chosen for experimental validation. An experimental setup was constructed, and several experiments were conducted to prove the different abilities of the proposed sensor. The proposed sensor demonstrated a threshold sensing limit of 3.4 mm/s in oscillatory flow sensing.

INDEX TERMS Artificial lateral line sensor, polyvinylidene fluoride (PVDF) membrane, flow sensing, underwater flow sensor.

I. INTRODUCTION

Underwater flow sensors are used to measure many different parameters in marine environments, such as the flow velocity, acceleration, pressure gradient, and shear stress of water. Flow sensing is an essential technology in marine sciences. Currently, there are many existing technologies for measuring the flow field, such as wheel flow meters [1], pressure sensors, hot-wire anemometry [2], acoustic Doppler velocimetry (ADV), and particle image velocimetry [3]. However, these technologies have certain limitations. For example, acoustic sensors suffer from scattering and multipath propagation problems [4]. Optic sensors cannot propagate well in water and are limited by the turbidity of the sea water [5]. Neither sensors is suitable for forming a distributed array. Because of these limitations, many researchers are trying to study new alternative sensors that are inspired by biological sensing abilities, such as the lateral line organ of fish.

The associate editor coordinating the review of this manuscript and approving it for publication was Roberto C. Ambrosio.

Most fishes are dependent on lateral organs to detect their surrounding environment [6], track prey [7], and communicate [8]. The lateral organ is composed of neuromasts, that are distributed on both sides of the fish body. Neuromasts are divided into two types according to their location: superficial neuromasts (SNs) and canal neuromasts (CNs) [9], [10], as shown in Fig. 1.

SNs are distributed over the surface of the fish body and interact directly with the external flow for flow velocity detection. In contrast to SNs, CNs are removed from direct external flow and submerged in fluid-filled canals for flow pressure gradient perception. These two types of lateral line systems rely on neuromasts. Each neuromast contained several hundred hair cells with hair-like cilia enveloped in a gelatinous cupula. The lateral line hair cells were morphologically polarized. A neuromast is a deflection sensor that works roughly like a cantilever beam that extends into the flow. When fluid passes the cupula, it causes the cupula to move, which in turn deflects the cilia of the hair cells, and the deflections are converted into neuron signals for the fish [11].

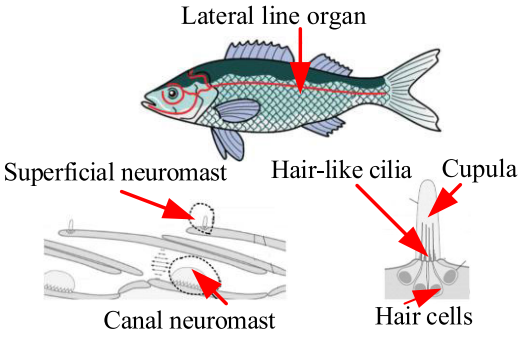

FIGURE 1. Distribution of lateral line organ.

Inspired by the astonishing flow-perception ability of lateral line organs, many researchers have developed various artificial lateral line sensors that emulate both SNs and CNs.

A. ARTIFICIAL SNs

Many researchers have developed artificial SNs based on different sensing mechanisms, including piezoresistive, capacitive, piezoelectric, and optical detection schemes.

Based on the piezoresistive effect, a hair-like artificial lateral-line system was developed [12]. The hair-like structure is a rectangular plate shape, and the material of the hair structure is a gold-permalloy composite. The piezoresistive material was boron-ion-diffused Si. In another design [13], the vertical hair was rigidly attached to the substrate, the lateral cantilever was omitted and a strain gauge was attached at the base of the hair. To improve spatial resolution, the hair structure adopted a symmetric cylindrical shape with a high aspect ratio and the material of the hair structure was SU-8 [14], [15]. In natural lateral line system, the cupula plays an essential role in the sensitivity of neuromasts. To mimic its biological counterpart, an artificial cupula with hydrogel encapsulation has been fabricated [16], [17].

An artificial flow sensor based on the capacitive principle was employed by the research group of transducer science and technology (TST) at the University of Twente [18], [19]. This fully supported flexible SU-8 thin membrane sensor was realized. The sensor integrates the electrodes underneath and the electrodes support cylindrical hair-like structures on top. The thickness of the thin layer was approximately 500–800 nm. The capacitors used were common flat parallel plates. Another biomimetic flow sensor based on the capacitive principle has also been reported [20]. The membranes had thin chromium electrodes on top, forming variable capacitors with the substrate, allowing for capacitive readout. The capacitive sensing principle was also employed [21] to develop a whisker-like artificial sensor that mimicked seal vibrissae. In this design, a rigid artificial whisker was mounted on a novel cone-in-cone parallel-plate capacitor base. The base was separated into four distinct quadrants, and covered by a polydimethylsiloxane (PDMS) membrane. The PDMS membrane can create the necessary damping and restoring forces, and the base divisions can determine fluid direction.

Piezoelectricity is the electric charge accumulated in certain solid materials in response to an applied mechanical load or deformation. Asadnia *et al*. developed a piezoelectric micro-diaphragm pressure sensor that performs passive fish-like underwater sensing [22]. To achieve high sensitivity at low frequencies, a high-quality Pb $(Zr_{0.52}Ti_{0.48})$ O3 (PZT) thin membrane was used as the piezoelectric material. It is not a hair-like sensor but is flexible and surface-mountable piezoelectric sensor. A novel bio-inspired artificial lateral line system was achieved by exploiting the inherent sensing capability of ionic polymer-metal composites (IPMCs) [23], [24]. An artificial hair sensor based on aligned suspended polyvinylidene fluoride (PVDF) fibers was designed using a novel fabrication method called the thermo-direct-drawing technique [25]. Using this method, submicron-diameter fibers were successfully fabricated on flexible Kapton. The separated electrodes were deposited along the fiber drawing direction. The poling of micro/nanofibers imparts good piezoelectric effectiveness. Preliminary validation experiments showed that this artificial hair sensor based on PVDF has a reliable response with good sensitivity to external pressure variation and, medium flow. Other efforts are also being undertaken to fabricate piezoelectric-material-based hair flow sensors [26]–[30].

Optical sensing principles have also been explored by researchers. Klein *et al.* developed an optical artificial lateral line system for determining the object position and, vortex shedding frequency [31]. Sebastian and Wolfgang [32] explored another sensor based on the optical sensing principles. This sensor is based on thin cylindrical structures, that bend owing to the exerted fluid forces. The pillar deflection was recorded using a high-resolution camera.

B. ARTIFICIAL CNs

Various pressure sensors inspired by the CNs of fish have been explored. A high-density array of pressure sensors has been developed for passive underwater navigation [33]. Yaul *et al.* explored a flexible artificial lateral-line pressure sensor using a conductive elastomer strain gauge [34]. Duesk *et al.* developed a prototype pressure sensor array fabricated from carbon black-doped silicone closed-cell foam [35]. Herzog *et al.* proposed a schematic setup and optical sensing mechanism for the sensor mimicking the canal system of the fish lateral line [36]. A flexible artificial lateral line canal system was developed for hydrodynamic pressure detection [37].

In this study, we developed an artificial lateral-line sensor using PVDF for oscillatory flow sensing. The sensor mimics the biological structure of the lateral line organ, including cupula, hair-like cilia, and hair cells. To mimic hair cells, we used a polyvinylidene fluoride (PVDF) membrane as the sensing element; because PVDF has excellent characteristics, such as its flexible mounting ability, wide frequency bandwidth, high strain sensitivity, and low cost [38]–[40]. In contrast to the traditional sensors only used in the laboratory, Our designed sensor considers the field environment.

In the next section, we design the sensor and discuss the influences of the typical parameters of the sensor on the sensing performance, such as the shape and, length of the cantilever beam. We also describe the 3D printing, assembly of the sensor, and waterproofing scheme used to protect the sensor from harsh fluid environments. In Section III, we describe the experimental setup and results, which are further discussed and interpreted. Finally, we share our perspectives on the technological challenges and future work.

II. DESIGN AND FABRICATION OF SENSOR

A. SCHEME OF SENSOR STRUCTURE

This study aims to design a new artificial lateral line sensor inspired by the existing structure of lateral line organ. The lateral organs are composed of neuromasts. The neuromast is composed of cupula, hair-like cilia, and hair cells. These cilia are attached to one end of the nervous system. When fluid passes the cupula, it causes the cupula to move, which in turn deflects the cilia of the hair cells and the deflections are converted into neuron signals for the fish. Based on the morphological structure and sensing principle of the neuromast, we propose a scheme for an artificial lateral line sensor, as shown in Fig. 2. This sensor is composed of an artificial cupula, cantilever beam, and perception unit.

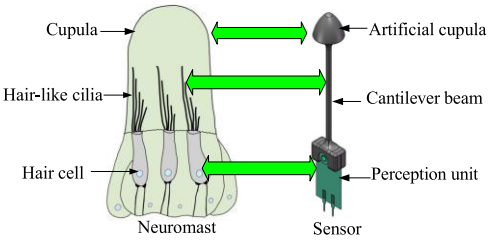

FIGURE 2. Scheme for an artificial lateral line sensor.

The artificial cupula mimics the cupula of neuromasts. It directly contacts the external water environment, senses the force generated by the oscillatory flow, and transmits the force to the cantilever beam. The cantilever beam mimicked hair-like cilia and was cylindrical. After receiving the force transmitted by the artificial cupula, the cantilever beam further transmitted the force to the perception unit. The perception unit mimics hair cells and uses a PVDF piezoelectric membrane as a sensing element. Its function is similar to that of hair cells under hair bundles in the neuromasts of fish. The perception unit was used for the final perception of flow information. One end of the perception unit was fixed to the tail of the cantilever beam, and the other end was fixed to the supporting base. The supporting base integrated electrodes underneath, which were connected to the amplifier circuit through wires.

B. FABRICATION OF SENSOR

The goal of this study was to design and fabricate an artificial lateral-line sensor using PVDF. In this process, the shape of the artificial cupula and the length of the cantilever beam are very important for sensing performance of the sensor. We used the computational fluid dynamics (CFD) and piezoelectric analysis methods to achieve a better solution for the shape of the artificial cupula and the length of the cantilever beam. Three-dimensional (3D) printing technology has been used to fabricate artificial cupula and cantilever beam. The PVDF is directly connected to the bottom of the cantilever beam, and the deflections are converted into voltage signals. Finally, we conducted waterproofing of the sensor to protect it from a harsh fluid environment.

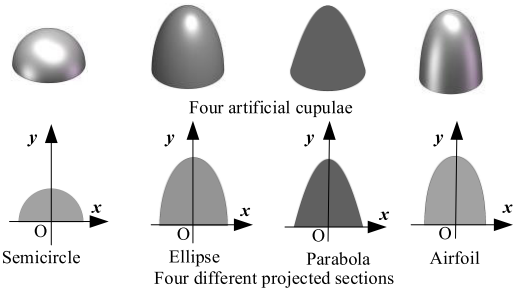

FIGURE 3. Four artificial cupulae.

1) SHAPE OF ARTIFICIAL CUPULA

We discuss four artificial cupulae with different projected-sectional shapes, such as semicircle, ellipse, parabola, and airfoil as shown in Fig. 3.

We compared the drag force on these four artificial cupulae in a flow environment. The final selected artificial cupula is guaranteed to be subjected to the maximum drag force at the same flow velocity. A shape with a larger drag force will help improve the sensitivity of the sensor.

In the simulation, the 3D geometry model of the artificial cupula was defined using the SOLIDWORKS application. To discuss the influence of shape, we should ensure the same project area for the four different artificial cupulae when creating the model geometry. The 3D models, as external geometry files, were imported to the DesignModeler application. Then, the enclosure tool of DesignModeler is used to enclose the 3D model so that the material enclosing the 3D model can be assigned to the fluid in the ANSYS for simulation. In the next section, a detailed setup is provided, including the

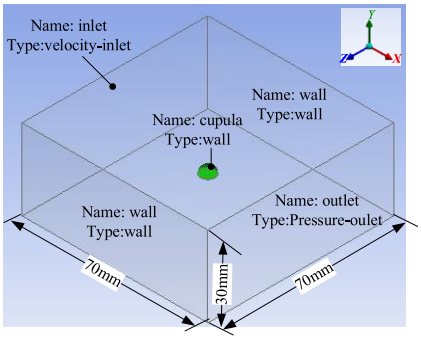

FIGURE 4. Geometry of the computed domain.

boundary and solver constraints, meshing strategy and turbulence modelling. The dimensions of the computed domain are shown in Fig. 4 and the boundary conditions are defined in the following section.

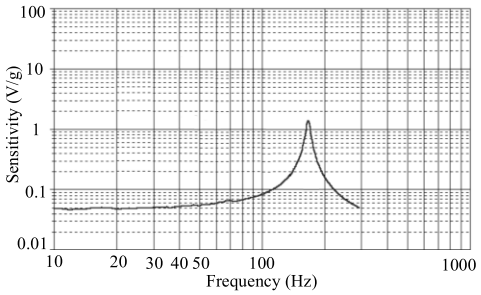

FIGURE 5. Sensitivity versus frequency of PVDF membrane.

Usually, in ambient natural flows, the flow velocity ranges from a few centimeters to several hundred centimeters per second. In order to set the physical conditions modelled to maintain consistency with the dipole experiments. We confined the inlet flow velocity condition to the scope of 0-0.65 m/s. For the problem of frequency, we used a commercial PVDF piezoelectric membrane, LDT0-028K, produced by Measurement Specialties Ltd. The sensitivity versus frequency plot of the commercial PVDF piezoelectric membrane is shown in Fig. 5 [41]. Therefore, the sensitivity is almost independent of the frequency when the frequency is less than 50 Hz, and LDT0 shows a resonance around 180 Hz. The frequency of the dipole experiments ranges from 10 to 50 Hz. Therefore, to simplify the numerical modelling process, only the amplitude of the velocity was considered in the numerical modelling conditions.

In this study, the flow velocity ranges from 0 m/s to 0.65 m/s and the cupula diameter at the base was 6 mm. From (1), we can obtain the Reynolds number (Re), which is less than 3900 (Re $<$ 3900).

$$Re = \frac{\rho VD}{\mu} \tag{1}$$

where, D is the diameter of the cupula at the base, ρ is the density of water (1000 kg/m^3), and μ is viscosity (0.001 kg/(m·s)). V is flow velocity.

In this study, a pressure outlet was applicable in all cases. For the pressure boundary, the relative pressure is set to zero. The sides were assigned as 'no-slip wall' boundaries. The cupula boundary was also set to a no-slip condition.

For turbulence properties, with low Re cases, re $<$ 160 or flow velocity of approximately 25 mm/s, Park *et al.* [42] and Dehkordi *et al.* [43] both obtained excellent agreement with experimental values for all parameters monitored using a laminar method. Moving into the subcritical regime, the research conducted by Rahman *et al.* [44] compared a number of two-equation turbulence models at Re values of 1000 and 3900. Rahman *et al.*'s results showed a clear improvement in accuracy using the shear stress transport model (SST) over the K-epsilon and realizable K-epsilon models. Stringer *et al.* [45] incorporated the SST turbulence model for flows with Reynolds numbers ranging from 40 to 10^6. According to the above results, in this study, the cases with low Re employ a laminar model whereas turbulent flows with Re $>$ 160, employ the shear stress transport turbulence model (SST).

TABLE 1. Basic configuration.

Items	Configurations
Fluid material	Water-fluid
Inlet	Velocity-inlet
X-velocity	0-0.65 m/s
Y-velocity	0
Outlet	Pressure-outlet
Gauge pressure	0
Wall	Wall
Turbulence model	Re<160: laminar; 160<Re<3900: SST model
Solver	SIMPLE

We performed an analysis using ANSYS Fluent. We used the SIMPLE scheme for velocity-pressure coupling. For the convection and diffusion terms, a first-order upwind scheme is adopted for the initial iterations followed by the second-order upwind scheme for the rest of the analysis. The convergence criterion for the residual of drag force was 1e-6. We chose a standard initialization. The initial values of the gauge pressure, y-velocity and z-velocity were set to 0. The basic configurations are listed in Table 1.

We used the mesh application in ANSYS to create the mesh. The physics preference was CFD, and the solver preference was set as Fluent. The curvature size function was selected to control how the mesh size was filled in the domain. The mesh attributes include the minimum size, maximum face size, and growth rate. On the other hand, the options of the boundary layer that we selected, such as the total layer thickness, maximum layers, and growth rate, also control the mesh. Therefore, the different sizing configurations of the mesh and the different options of the boundary layer result in different numbers of nodes and elements.

The value of y+ is dependent on the resolution of the mesh and Reynolds number, and is defined only in wall-adjacent cells. The y^+ value represents the non-dimensional distance of the first node from a no-slip wall. It links the node distance to the shear stress by a nondimensional value with the fluid properties. It is generally accepted that the mesh must achieve a first-layer cell thickness equivalent to $y^+ < 1$ for most solvers (see ANSYS [46] and Benim *et al.* [47]). We should check that the y^+ of the wall-adjacent cells is on the order of $y^+ = 1$. In this study, the final meshes conformed to a maximum value of $0.5 < y^+ < 1.5$ on post-processing. Otherwise, we modified our mesh.

To achieve high-level grids, we define the final mesh attributes that are confirmed after mesh sensitivity studies for different flow velocities and different artificial cupulae.

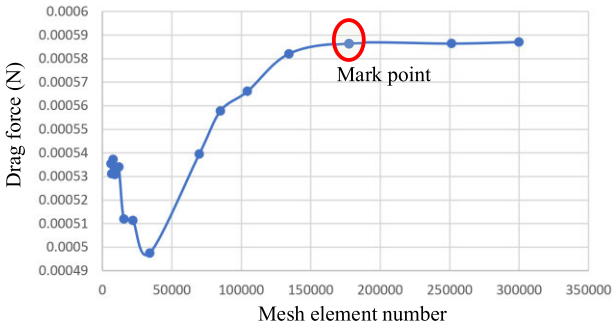

FIGURE 6. Mesh sensitivity analysis.

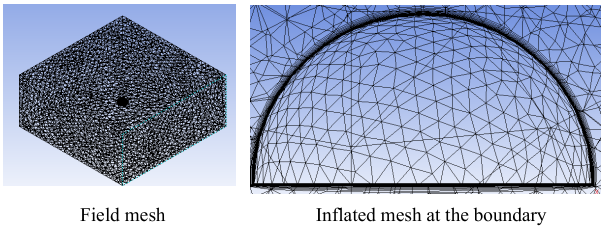

FIGURE 7. A typical mesh (0.4 m/s and semicircle cupula).

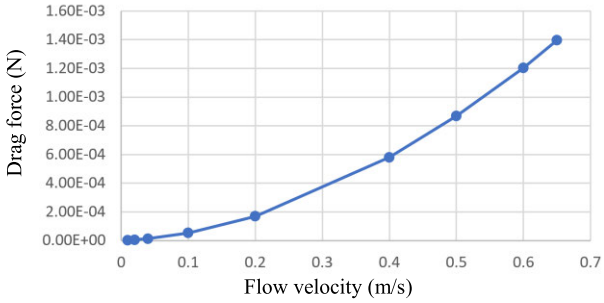

FIGURE 8. Drag force versus flow velocity (semicircular cupula).

A CFD solution cannot be trusted unless we check whether the result depends on the mesh. The results of coarser and finer mesh cannot be the same. Therefore, we must vary the mesh to obtain the accepted level of tolerance, which can be determined from the mesh sensitivity analysis. This was done by varying the mesh size from coarse to fine, and checking the output results for each mesh. When varying the mesh does not significantly affect the result, we can stop and select the minimum mesh size for the final solution. We performed a mesh sensitivity analysis using the parametric analysis method. First, we created the input parameters for meshing. Second, we set up the output parameters using Fluent. Finally, we compared the results of various mesh sizes starting from coarse to fine. The following case is for mesh sensitivity studies when flow velocity is 0.4 m/s for the semicircle cupula.

As shown in Fig. 6, the result variations are not significant after the marked point. Hence, this can be considered a better mesh for the calculation. This mesh size provides better results in less time as compared to a finer mesh. The final

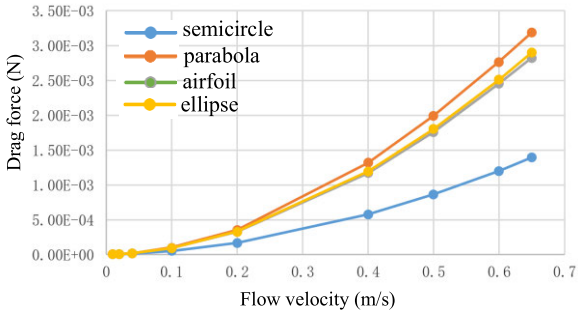

FIGURE 9. Drag force versus flow velocity.

mesh, which was confirmed after mesh sensitivity and y+ adaptation, is shown in Fig. 7.

The left side of Fig. 7 shows the image of near- and far-field meshes from the cupula, and the right side of Fig. 7 shows the details of the inflated mesh at the boundary of the cupula. In this case, the element number was 1.75e+5, the maximum thickness of the boundary layer was 0.17mm, the number of layers was 20 and the result of y+ was 1.3.

Repeating the above calculation process, we calculated again at different flow velocities or Reynolds numbers for the semicircle cupula. Fig. 8 shows the drag force at different flow velocities for the semicircular cupula.

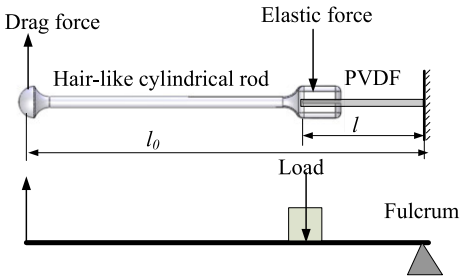

FIGURE 10. Lever model of sensor.

We again calculated for other three artificial cupulae. Thus, we obtained the drag force at different flow velocities for these four artificial cupulae. The curves of the final results are shown in Fig. 9.

From Fig. 9, for the same projected area of different shapes, we observe that the drag force of the parabolic shape is slightly larger, and it can sense effectively the flow velocity compared with the semicircle, ellipse, and airfoil. Based on the results, we chose a parabolic shape for the artificial cupula.

2) LENGTH OF CANTILEVER BEAM

With the exception of an artificial cupula, we designed a cantilever beam with high aspect ratio and cylindrical hail-like structure that mimics hair-like cilia. The beam length was selected by comparing the output voltages. During this process, the noise of the amplifier circuit must be considered simultaneously. Considering the length constraint of sensor to reduce the impact on fluid caused by the length of beam, the

length of the cantilever beam ensures that the output voltage of sensor is greater than the circuit noise, which determines the threshold of sensor. As described above, the hair-like cantilever beam transmits the drag force on the cupula to the piezoelectric unit. The structure can be modelled as a lever, as shown in Fig. 10.

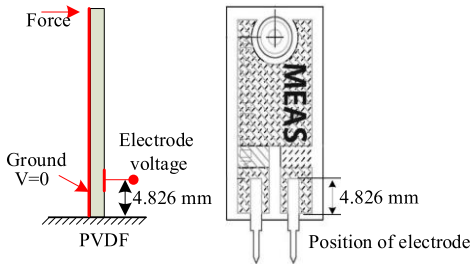

FIGURE 11. PVDF and position of electrode.

TABLE 2. Material properties for PVDF.

Items	Configurations
Young's modulus	$2.0\times 10^{9}(N/m^{2})$
Poisson's ratio	0.29
Shear modulus	$0.775\times 10^{9}\ (N/m^{2})$
Piezoelectric strain coefficients d_{31}	2.2×10^{-11} (C/N)
Piezoelectric strain coefficients d_{32}	0.3×10^{-11} (C/N)
Piezoelectric strain coefficients d_{33}	-3.0×10^{-11} (C/N)
Relative permittivity at constant stress	12
Density	1870 (Kg.m^{-3})

Thus, the drag force acting on the artificial cupula was considered as the effort and the elastic resistance force due to the deflection of the PVDF piezoelectric unit was considered as the load. According to the lever law:

$$F_{elastic} = \frac{F_{Drag} \times l_0}{l} \tag{2}$$

where: $F_{elastic}$ is the elastic resistance force, F_{Drag} is the drag force acting on the artificial cupula, l is the length of the PVDF piezoelectric unit, l_0 is the total sensor length. Because the force acting on the PVDF piezoelectric unit is the opposite of the elastic resistance force, these two forces are equal, but in the opposite direction. Thus, the magnitude of the force acting on the perception unit is calculated.

$$F = F_{elastic} \tag{3}$$

After achieving the force on the perception unit, we could used ANSYS APDL software to complete the piezoelectric analysis. PVDF is widely used as a piezoelectric membrane for sensing applications. In sensing mode, the PVDF membrane was used to measure the external load by monitoring the piezoelectrically induced electrode voltages. As shown in Fig. 11, this is a piezoelectric analysis of a PVDF membrane mounted as a cantilever, with the bottom of the PVDF perception unit fixed. The left surface of the PVDF had one electrode patch and the right surface was grounded. The right

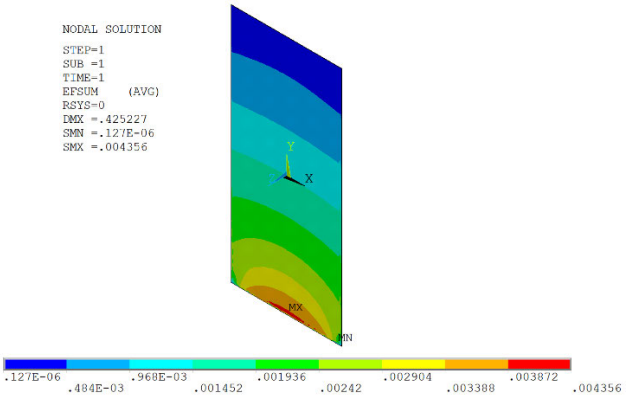

FIGURE 13. Piezoelectric nephogram (l = 60 mm and V = 0.4 m/s).

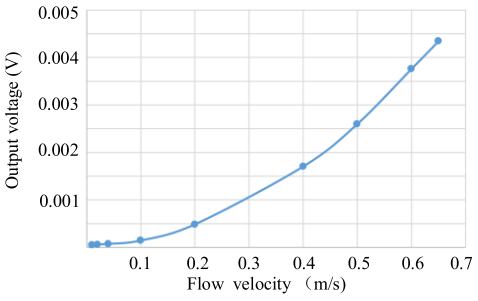

FIGURE 14. Output voltage (length = 60mm).

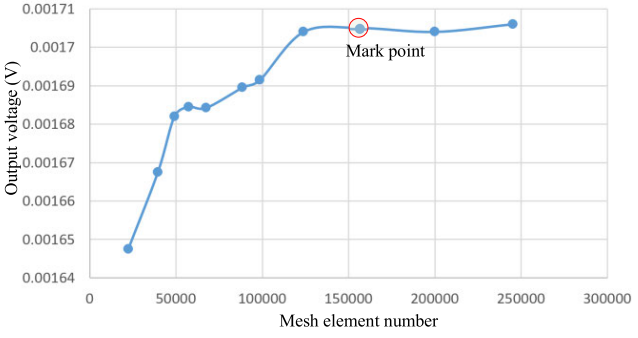

FIGURE 12. Mesh sensitivity for piezoelectric analysis.

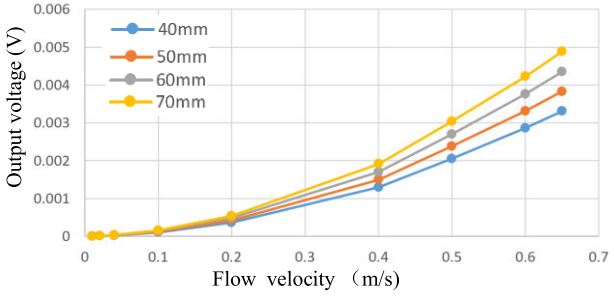

FIGURE 15. Output voltage of the different beam length.

side of Fig. 11 shows the commercial PVDF piezoelectric membrane, LDT0-028K. According to the actual position of the electrode on the PVDF membrane, we obtained the output voltage at the same position as piezoelectric nephogram.

In the piezoelectric analysis process, we defined the material properties of PVDF, such as the piezoelectric constant, dielectric constant and other properties of the PVDF perception unit, as shown in Table 2.

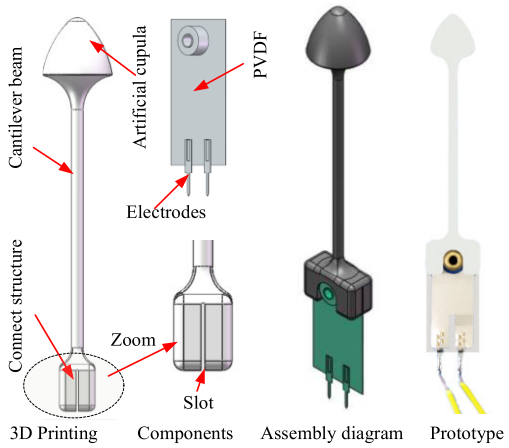

FIGURE 16. 3D printing and assembly process of sensor.

We built a finite element model of the PVDF according to the material properties including the coordinate system, elastic compliance matrix, and piezoelectric strain matrix. Subsequently, we generated a mesh within the PVDF. We also defined the final mesh attributes that were confirmed after mesh sensitivity studies, as shown in Fig. 12.

In this case for mesh sensitivity analysis, the flow velocity was 0.4 m/s, and the length of the cantilever beam was set to 60 mm for the parabolic cupula. We compared the results of various mesh sizes, starting from coarse to fine. As shown in Fig. 12, the result variations are not significant after the marked point; hence, this can be considered a better mesh for the calculation.

The final piezoelectric analysis results are shown in Fig. 13. An output voltage of 0.002904 V was obtained at actual electrode position of the piezoelectric nephogram. Considering that gain of the charge amplifier was 100, the final simulation voltage output of sensor is 0. 2904 V, which is very close to the results of the actual flow-velocity-sensing experiments described in Section III.

The process is repeated again, and the output voltage can be obtained at different flow velocities when the beam length is 60 mm. The results are shown in Fig.14.

Then, the process is repeated at different cantilever beam lengths in the same manner. The lengths of the cantilever beams were be set to 40mm, 50mm, and 70mm. The results are shown in Fig. 15.

It can be seen that the output voltage of the sensor increases with the length of the beam. The length of the beam should be selected according to the target threshold of the sensor and circuit noise. The circuit noise was approximately 1.5 mV, the gain of circuit was 100 in the actual experiments, and the target threshold is set to 3 mm/s. It was necessary to ensure that the output voltage at the target threshold (3 mm/s) was greater than the circuit noise. For beams with lengths of 40, 50, 60, and 70mm, only the output voltages of beams with lengths of 60 and 70 mm are greater than the circuit noise in the simulation process. Considering the length constraint of the sensor to reduce the impact of the length of beam on fluid, a beam with a length of 60 mm was selected.

TABLE 3. Structural parameters of final sensor.

Component	Type	Size
Artificial cupula	shape	parabolic shape
	thickness	6 mm
Cantilever beam	diameter	2 mm
	length	60 mm
PVDF	length	25 mm
	width	11 mm
	thickness	0.4 mm

3) 3D PRINTING AND ASSEMBLY OF SENSOR

A schematic of the assembly process and the prototype of the real sensor without waterproof processing are shown in Fig. 16. At the end of the beam, a connected structure was designed to connect the beam to PVDF piezoelectric unit. As shown in magnified picture in Fig. 16, at the end of the beam, there is a slot at the bottom. Thus, a PVDF piezoelectric unit can be inserted into this slot and connected to the beam.

The artificial cupula and cantilever beam used the same resin material, which is lightweight and excellent elasticity. We fabricated an artificial cupula and high-aspect-ratio beam, which was approximately 60 mm tall and 2 mm in diameter, using the 3D printing process. At present, a large number of 3D printing processes are available, and the main differences between processes are in the way that layers are deposited to create parts and materials that are used. We used the 3D printing process called fused filament fabrication, also

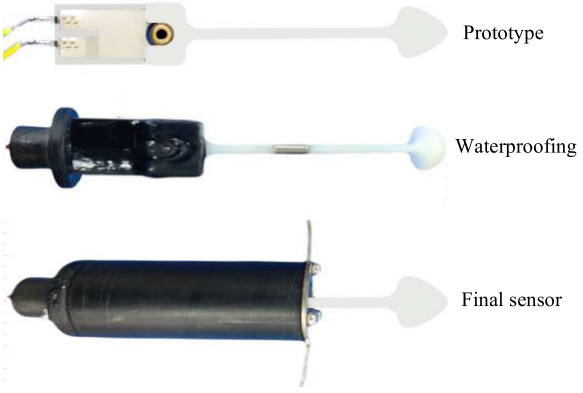

FIGURE 17. Final sensor with protect shell.

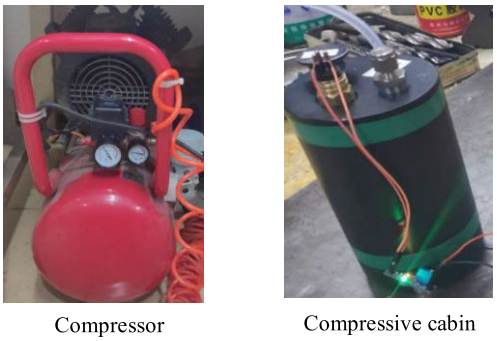

FIGURE 18. Waterproofing experimental setup.

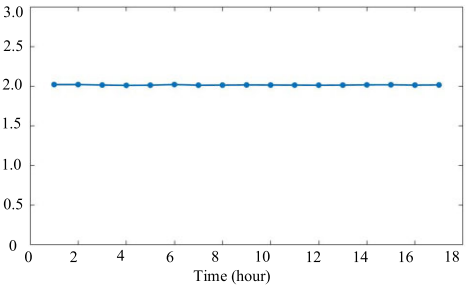

FIGURE 19. The results of waterproofing experiment.

known as fused deposition modelling. We used the 3D printer CR-2526, which was produced by ShenZhen CREALITY 3D Ltd. The printing speed was approximately 60-90 mm/s and the printing accuracy was ± 0.1mm. We created 3D printable models using the SOLIDWORKS package and saved the CAD models in the stereolithography file format (STL) as input files for the 3D printer.

A commercial PVDF piezoelectric membrane is used as the perception unit, which is the LDT0-028K produced by Measurement Specialties Ltd. It is a flexible component comprising a 28 μm thick piezoelectric PVDF polymer membrane with screen-printed Ag-ink electrodes, laminated to a 0.125 mm polyester substrate, and fitted with two crimped

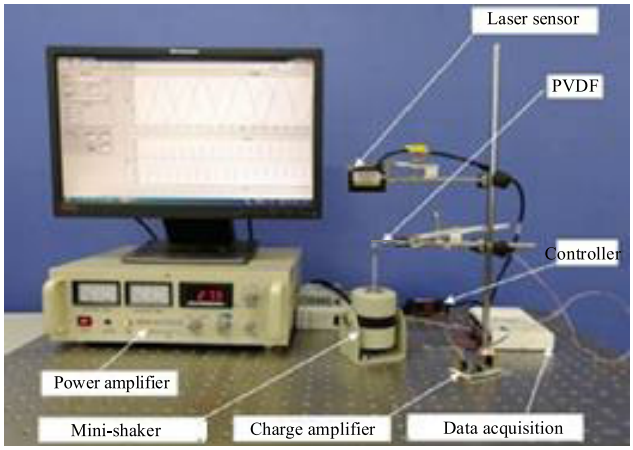

FIGURE 20. The vibration experimental setup.

contacts. According to the processes mentioned above, the final structural parameters of the sensor were determined, as shown in Table 3.

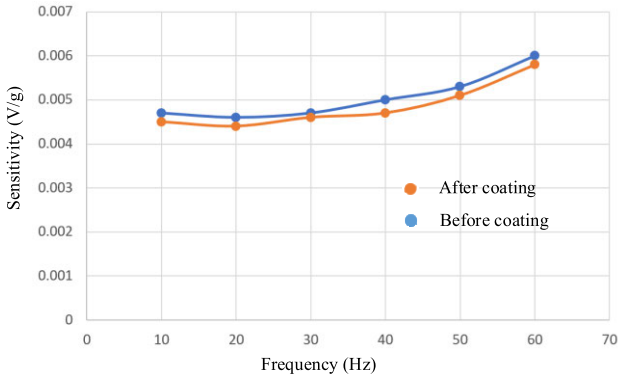

FIGURE 21. Frequency response before and after coating.

4) WATERPROOF AND PROTECT SHELL

Significant, progress has been made in the research on artificial lateral line sensors. However, because of waterproofing, most sensors are limited to the laboratory environment and not suitable for a real marine environment. Therefore, commercial pressure sensors are widely used to simulate artificial lateral line sensors. Waterproofing schemes for underwater applications are important in practical applications. A well-designed waterproofing scheme is required to protect the sensor from harsh fluid environments. To resist the ingress of water and the sensor may be used underwater to specified depths, parylene C and epoxy resin are used for sealing and waterproofing purposes. To waterproof the PVDF membrane, a parylene C conformal coating was deposited by room-temperature chemical vapor deposition [48]. The thickness of the parylene layer is 2 μm. The parylene coating layer, which was virtually unstressed, did not affect the bending, but affected its stiffness. The cable joint, fixed end, and fixed structure of the sensor used the epoxy resin for waterproofing. After the epoxy process, the entire sensor was left at room temperature for 24 h for slow drying. To facilitate installation on the body, such as an AUV, and for the purpose of protection, a shell is designed around the sensor. The sensor was then inserted into the protective shell cavity. The final sensor with waterproofing encapsulation and shell is shown in Fig. 17.

The water-resistant performance was validated using waterproofing experiment. The experimental setup is shown in Fig. 18. The experimental setup included a compressor and compressive cabin.

Here, the working depth of the sensor was set to 30 m, so the maximum pressure was set to 0.3 MPa. Here, the maximum pressure (0.3MPa) was a gauge pressure, which was the pressure relative to the ambient pressure. In the experiment, the sensor was placed in a water-filled compressive cabin. The gauge pressure was adjusted to 0.3 MPa. The voltage was continuously measured. The duration was more than ten hours, and the results are shown in Fig. 19.

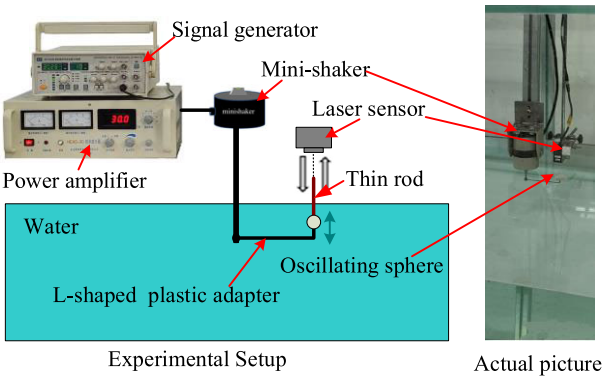

FIGURE 22. Experimental setup for calibrating.

It can be seen that the output value remain stable, which proves that the waterproofing effect of the sensor is good.

To compare the frequency response before and after the coating, we conducted a vibration experiment. The experimental setup is shown in Fig. 20.

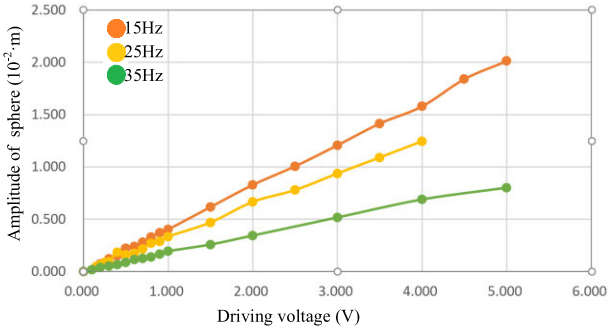

FIGURE 23. Results of calibration experiment.

The vibration experimental setup included three units: the excitation unit, excitation input signal measurement unit and data acquisition unit. One end of the PVDF was fixed on the stainless-steel support, and the other end of the PVDF was fixed on the end of the exciter to vibrate with the exciter. We measured the vibration acceleration signal at the end of the PVDF by an excitation measurement unit using a CMOS laser sensor (IL-S025, KEYENCE). We also read the output voltage of the PVDF through a data acquisition unit (USB-6210). The original data were transformed using FFT to calculate sensitivity. We compared the sensitivity of PVDF before and after coating, as shown in Fig. 21. The coating reduces "baseline" sensitivity slightly. Therefore, the coating has little effect on the sensing properties.

III. OSCILLATORY FLOW SENSING

The dipole stimulus was chosen for the flow-sensing experiments because the flow field generated by an oscillating sphere has been well studied and has been used by other researchers in the past for characterizing sensors [49]–[51].

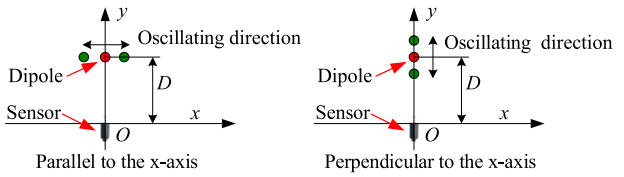

FIGURE 24. 2-D minimal model.

A. CHARACTERIZATION OF DIPOLE FLOW FIELD

We characterized the flow field before testing the sensor response to the oscillatory flow velocity.

1) CALIBRATION OF OSCILLATING SPHERE

To characterize the dipole field, we first calibrated the relationship between the output driving voltage of the signal generator and the displacement amplitude of the oscillating sphere. Then, we can calculate the flow velocity at any observation distance or position of the sensor using the model of dipole flow field. Typically, a sphere is attached to a small rod driven by a mini-shaker that generates small vibrations. Equal input voltages fed into the mini-shaker may lead to different amplitudes of the sphere across stimulus frequencies. Consequently, the amplitudes of the sphere were measured across frequencies prior to the experiments. We performed the calibration in water and the experimental setup for calibration is shown in Fig. 22.

Because the mini-shaker and laser sensor are not waterproof, a small plastic adapter with an L-shape is positioned between the shaker axis and the sphere. Meanwhile, we rigidly fixed an extremely thin and light rod at the center of the sphere. Therefore, the amplitude of the sphere in water can be obtained by measuring the amplitude at the tip of the rod. Thus, the mini-shaker and laser sensor could be fixed in air. In the experiment, the signals were amplified by a specified gain of 20 dB through a power amplifier (HEAS-2), and a laser sensor (IL-S025, KEYENCE) was used to measure the displacement. The experiment was repeated for different driving voltages and stimuli frequencies. The displacement of the oscillating sphere in the time domain was processed using the FFT operation to achieve the amplitude of the oscillating sphere. The results for 15, 25, and 35 Hz are shown in Fig. 23.

It is evident from Fig. 23 that the amplitude of the oscillating sphere exhibits an approximately linear response to the

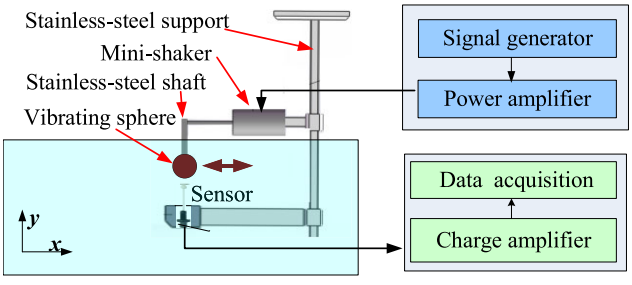

FIGURE 25. Schematic diagram of the experimental setup.

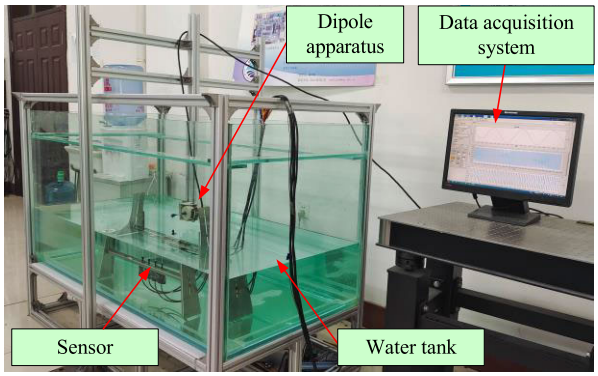

FIGURE 26. Actual experimental platform.

varying driving voltage of the signal generator at a constant frequency and the result is similar to those in the literature [49], [50]. Thus, the oscillating sphere can be driven at the desired amplitude and frequency and controlled by a signal generator connected to a mini-shaker.

2) MODEL OF DIPOLE FLOW FIELD

We inferred the displacement amplitudes of the sphere from the results of the calibration experiment, as discussed in the previous section. Next, we need the theoretical formula of the dipole flow fields to obtain the flow velocity at any observation distance or sensor position.

The theory of dipole flow fields has been extensively studied in the past [52], which allows us to obtain the flow velocity at any observation distance. For simplicity, we neglected the water displacements that occur owing to gravity, temperature differences, and rotational motion, but only considered the flow generated by the movement of the dipole. Fig. 24 shows the schematic of the model. The lateral line sensor is arranged on the x-axis. The oscillating sphere is located at position (0, D). It oscillates parallel or perpendicular to the x-axis, generating a dipole velocity field.

For a sphere at a position that oscillates parallel to the x-axis and in the plane of the sensor, the dipole flow field

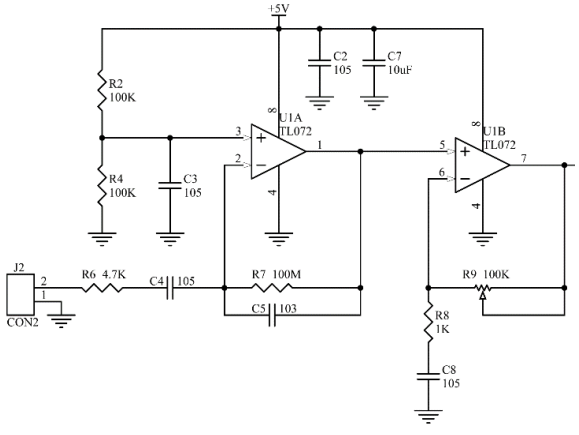

FIGURE 27. Charge amplifier and voltage amplifier.

at any observation distance along the x-axis can be described as the follows [52].

$$v_x\,(x, y = 0, t) = \frac{\mu(t)}{2\pi} \times \frac{2x^2 - D^2}{\left(x^2 + D^2\right)^{5/2}} \tag{4}$$

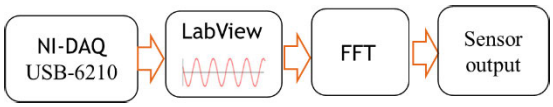

FIGURE 28. Data-processing process.

In the case of a sphere oscillating perpendicular to the x-axis in the plane of the sensor, that is, in the direction of the y-axis, the dipole flow field along the x-axis can be described as the follows [52].

$$v_x\,(x, y = 0, t) = \frac{3\mu(t)}{2\pi} \times \frac{Dx}{\left(x^2 + D^2\right)^{5/2}} \tag{5}$$

where $\mu\,(t) := 2\pi\omega sa^3 \sin(\omega t)$, ω is the angular vibration frequency, a is the sphere radius, s is the sphere amplitude of oscillating sphere, D is the distance between the center of the sphere and sensor, and x is distance along the x-axis. After the displacement amplitude of the sphere is calibrated, the flow field is obtained at any observation position from (4) and (5) in both the cases described above.

B. EXPERIMENTAL SETUP

This section introduces the experimental setup for validation of the sensor. The results of the experiment are also discussed to determine the performance of the sensor for oscillatory flow velocity sensing. A schematic of the experimental setup is shown in Fig. 25.

As shown in Fig. 25, the dipole oscillates along the x-axis. The mini-shaker was positioned horizontally and oscillated parallel to the x axis. The mini-shaker was mounted on top of a water tank using a stainless steel support structure, and the sensor was installed directly below the oscillating sphere. The experiments using an artificial lateral line sensor with PVDF were conducted in a water tank. The actual experimental platform is shown in Fig. 26.

The water tank consisted of dipole apparatus. This dipole apparatus generates oscillatory flow for sensing. A sphere with a radius of 23.5 mm was used as the dipole source, and this sphere was attached to the end of a mini-shaker (HEV-20) via a stainless-steel shaft. A mini-shaker with a maximum displacement of $\pm$ 10 mm and a wide frequency range from 10 to 50 Hz was used to drive the dipole at the desired frequencies and amplitudes in our experiments. The desired amplitude and frequency were controlled by a signal generator based on the characterization of the flow field discussed in Section III-A. The signal from the signal generator was amplified by a specified gain using a power amplifier (HEAS-2). A power amplifier is used to drive the mini-shaker. The water tank was 1500 mm long, 1000 mm

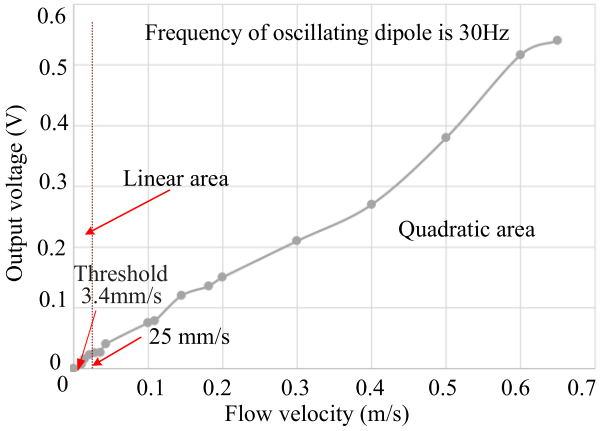

FIGURE 29. Voltage output at 35 Hz.

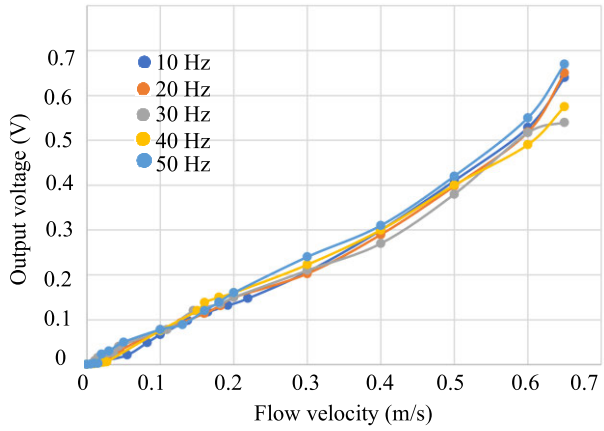

FIGURE 30. Flow velocity sensing at different frequencies.

wide and 700 mm deep. The thickness of the glass of the water tank was 15 mm with high hardness. The support frame and water tank are isolated from each other and do not come into contact to avoid noise caused by vibration.

The PVDF sensor generates a charge output signal with a very high impedance. To process this signal, it must be transformed into a low-impedance voltage signal. A charge amplifier is used for this purpose, as shown in Fig. 27.

The amplifier offsets the input current using a feedback reference capacitor C_5, and produces an output voltage that is inversely proportional to the value of the reference capacitors but proportional to the total input charge during the specified time period. Therefore, the circuit acted as a charge-to-voltage converter. The circuit gain depends on the value of the feedback capacitor. An op amp with negative feedback was used for a low-impedance voltage signal from the charge amplifier. The gain of the voltage amplifier depends on the feedback resistors, R_8 and R_9. In the flow velocity sensing experiment, the gain of the voltage amplifier was set to 100 by adjusting resistors R_8 and R_9.

The voltage output from the voltage amplifier was continuously monitored using a National Instruments (Austin, TX, USA) data acquisition system (NI-DAQ NI USB-6210) and

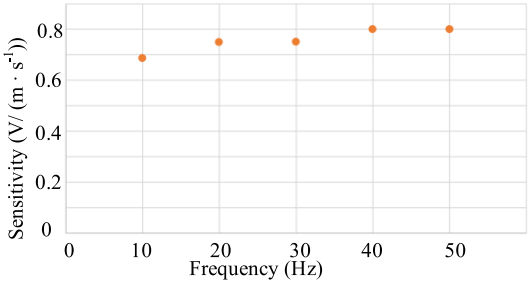

FIGURE 31. Sensitivity at different frequencies.

recorded using NI Signal Express software. To characterize the flow-sensing performance of the sensor, a simple data-processing method is proposed. Because we focused on a single sensor rather than a sensor system or array, and we wanted to determine the output voltage response of the sensor to dynamic flow stimuli, the fast Fourier transform (FFT) operation was used in this experiment. The data-processing process is shown in Fig. 28.

TABLE 4. Summary of the differences of several sensor.

Type	Depth in water	Threshold	Sensitivity
McConney et al. [53]	Not available	75 mm /s	122mV/(mm·s^{-1})
Asadnia et al. [50]	Not available	8.2 um /s	22 mV/(mm·s^{-1})
Zhang et al. [49]	Not available	4 mm/s	1.16 mV/(mm·s^{-1})
Asadnia et al. [22]	Not available	0.3mm/s	0.092mV/(mm ·s^{-1})
Bora et al. [54]	Not available	5 mm/s	45.2mV/(mm ·s^{-1})
Our sensor	30 m	3.4 mm/s	0.75mV/(mm ·s^{-1})

The voltage output was recorded using LabView, the voltage-time data were processed using the fast Fourier transform (FFT) operation in Matlab, and the FFT peak was noted as the sensor output and plotted against the oscillatory flow velocity amplitudes.

C. EXPERIMENTAL RESULTS AND DISCUSSION

Flow velocity sensing experiments are presented in this paper, which demonstrate the abilities of the proposed sensor using PVDF. The flow velocity sensing experiment demonstrated the sensitivity and threshold detection limits of the sensor in water. First, stimuli were generated using an oscillating sphere attached to a mini-shaker (type HEV-20). The displacement amplitudes of the sphere were inferred from the results of the calibration experiment of the oscillating sphere according to Section III-A-1. Second, referring to (4) or (5), the flow velocity is obtained at any observation distance according to dipole flow field model in Section III-A-2.

Third, the response of the sensor to various flow velocities generated by the oscillating dipole is measured.

1) EXPERIMENTAL RESULTS

The response of the sensor to various flow velocities generated by an oscillating dipole was measured. Fig. 29 shows the experimental results of flow sensing in water under various flow velocities. In this case, the frequency of the oscillating sphere is 30 Hz, the sensor is located directly below the oscillating dipole at a distance of 19.75 mm, and various flow velocities can be obtained by changing the displacement amplitude of the oscillating sphere.

It can be observed that the voltage output of sensor increased linearly with increasing flow velocity up to 25 mm/s ($Re \approx 160$). At higher flow velocities, the relationship between the voltage output of the sensor and the flow velocities was approximately quadratic. This is because, for lower flow velocities, the drag force generated by the skin friction on the artificial cupula of the sensor is the major contributor to the output of the sensor, which increases linearly with increasing flow velocity. However, at higher velocities, the pressure gradient dominated the overall contribution to the output of the sensor. In our experiments, the sensor demonstrated a threshold sensing limit of 3.4 mm/s in water flow velocities when the frequency of the oscillating dipole was 30 Hz.

Similarly, we changed the frequency of the oscillating dipole. We repeated the measurements at different frequencies. The curves of the final results are shown in Fig. 30.

We observed that the relationships between the voltage output of the sensor and the flow velocities were similar at different frequencies in the range of 10-50 Hz. According to the results shown in Fig. 30, we can obtain the sensitivities of different frequencies at a specific flow velocity. For example, the sensitivity is about 0.75 V/ $(\mathrm{m} \cdot \mathrm{s}^{-1})$ in sensing water flow velocities when flow velocity is 0.2 m/s and the gain of the amplifier circuit is 100, which is shown in Fig. 31. Therefore, we obtained a flat frequency response, and the sensor demonstrates that the sensor's response is independent of the frequency for the range of 10-50 Hz in the oscillatory flow sensing, which is consistent with the results reported in the literature [50].

2) DISCUSSION AND COMPARISON

We conducted a flow velocity sensing experiment to demonstrate the abilities of the proposed sensor using PVDF. This flow velocity sensing experiment demonstrates the sensitivity of 0.75 V/ $(\mathrm{m} \cdot \mathrm{s}^{-1})$ when the gain of the amplifier circuit is 100 and threshold detection limit is 3.4 mm/s, respectively, for an oscillating dipole stimulus vibrating at 30 Hz in water. In addition, the results show that the response of the sensor is independent of the frequency in the range of 10-50 Hz.

Inspired by the astonishing flow-perception ability of lateral line organs, many scientists have developed various artificial lateral line sensors. Here, we summarize the performance of other lateral line sensors created by other scientists, juxtaposed with our job, as following Table 4.

In contrast to other scientists, we considered the waterproofing of the sensor and our sensor is not only suitable for the laboratory, but also can be used in a real marine environment.

For some commercial flow measurement devices, for example, FlowTraker2 is an acoustic Doppler velocimeter (ADV), which is produced by SonTex and demonstrates a threshold sensing limit of 1 mm/s in water. Depth ranged from 0 to 10 m. The velocity accuracy is about $\pm 1\%$ when measured velocity is ± 0.25cm/s [55]. Compared with artificial lateral line sensor, the commercial devices are not suitable for forming distributed arrays and power consumption are high, such as ADV and PIV. Therefore, the artificial lateral line sensor is a useful supplement for commercial devices.

IV. CONCLUSION AND OUTLOOK

Inspired by biological research on superficial neuromast, we designed an artificial lateral line sensor using PVDF for oscillatory flow velocity sensing. To develop such an artificial lateral line sensor, we fabricated an artificial cupula that mimics the cupula of neuromasts, a cantilever beam that mimics hair-like cilia, and a perception unit using PVDF, which mimics hair cells. To achieve a better solution for the shape of the artificial cupula and the length of the cantilever beam, we used the computational fluid dynamics (CFD) and piezoelectric analysis methods. Therefore, we used 3D printing technology to fabricate an artificial cupula and cantilever beam. A well-designed waterproofing scheme was also proposed to protect the sensor from harsh fluid environments. Experiments of the proposed sensor for oscillatory flow velocity sensing were performed underwater by employing a dipole as the stimulus. The proposed sensor demonstrates flow sensitivities of 0.75 V/ $(\mathrm{m} \cdot \mathrm{s}^{-1})$ with threshold velocity detection limits as low as 3.4 mm / s in sensing water flows.

However, our study needs to be improved. In the calibration experiment of the oscillating sphere, although this experiment was carried out in water, considering that the mini-shaker and laser sensor were not waterproof, we added some auxiliary structures, such as L-shaped structure and thin rod. This is an indirect measurement rather than a direct measurement. In this respect, Herzog *et al.* have developed a high-quality, low-cost device that they termed a ''Smart Mechanical Dipole'' [56]. It provides real-time measurements of sphere acceleration along three axes and can be used to obtain an accurate stimulation trace. This article is of great value to us for future work.

We need to improve further work in the future. We used the theoretical formula of dipole flow fields to obtain the flow velocity at any observation distance. The main reason is that the sampling rate is generally approximately a few hertz for most ADVs; for example, the FlowTracker2 ADV is an acoustic Doppler velocimeter that is designed to perform point velocity measurements in water. This ADV has a variety of sampling rates of approximately 1, 2, 5, or 10 Hz [55],

while the frequency of our dipole experiments ranges from 10 to 50 Hz. Therefore, we did not use ADV in this experiment. PIV systems, such as the V3V-Flex Volumetric PIV system, are the most flexible and powerful systems with high temporal or spatial resolution for flow research. Although this method using a dipole flow field model that has been adopted by other researchers [49]–[51], it would be interesting to see measurement results from common flow measurement devices such as PIV at observation distances in the future.

In the future for expansion on this research, we will discuss the fluid-structure interaction for capturing the dynamic behavior of the sensor, and explore a dynamic, physical-based model for sensor using PVDF. Sensor modelling should be used to optimize the design of the sensor.

In the future, we plan to build an artificial lateral array system based on the current work. At present, there are two types of artificial lateral line systems, one uses the pressure sensor array to mimic canal neuromasts and the other uses a hair-like artificial lateral line system to mimic superficial neuromasts. For some artificial lateral line systems using pressure sensors, Tang *et al.* [57] introduced a near field detection system for an underwater robot based on a fish lateral line, and an array of pressure sensors was developed and installed on the surface of an underwater vehicle. Eight pressure sensors were used to build the array, and the resolution was approximately 0.0036 Mbar. Fernandez *et al.* [33] fabricated a lateral-line-inspired MEMS array pressure sensor for passive underwater navigation with a pressure resolution of approximately 1 Pa. Yaul *et al.* reported a flexible sensor array [34] with pressure resolution of 1.5 Pa. Krieg *et al.* [58] presented an intelligent distributed sensing system inspired by the lateral line found in fish to directly measure the fluid forces acting on vehicles, and which reduces position tracking errors by as much as 72% compared to a standard position error feedback controller. For some artificial lateral line systems based on a stem (mimicking a cantilever beam), Wolf *et al.* [59], [60] presented a 2D-sensitive artificial lateral line comprising eight all-optical flow sensors, which were used to measure the hydrodynamic velocity profiles along the sensor array in response to moving objects in their vicinity. Their average localization error was 0.72 cm using a recurrent neural network while the localization error was 4.27 cm using a feed-forward neural network. DeVries *et al.* [61] presented a lateral line consisting of two types of sensing modalities, an IPMC flow sensor, and a pressure sensor. They designed and constructed a robotic fish prototype that was outfitted with eight IPMC sensors and four embedded pressure sensors. Several other artificial lateral line systems for hydrodynamic sensing have been briefly reviewed in literature [62]. According to the above description, to further provide valuable underwater applications, it would be interesting to develop a sensor array to fabricate an artificial lateral line sensor system to improve the underwater situational awareness. To translate the artificial lateral line sensory system for AUVs, Triantafyllou *et al.* [63] investigated unsteady flow mechanisms that are employed by animals and posed some basic questions, such as how detectable is a flow from a localized distributed array. They also conducted experiments to examine how identifiable the flow is under both object detection scenarios [64]. During this process, the sensor data processing method is acknowledged to be as important as the physical artificial lateral sensory system. For example, Lakkam *et al.* [65] proposed a data-driven model that uses artificial neural networks to process flow data originating from a stationary sensor array located away from an obstacle placed in a potential flow. Therefore, data processing of sensory array is also very important and needs to be solved in the future.

The lateral line of fishes consists of two types of sensing elements: superficial neuromasts, which measure local flow velocities, and canal neuromasts, which measure approximate pressure gradients. Thus, in the future, we plan to develop an artificial lateral line composed of two types of sensors to enhance situational awareness. It provides a good prospect for AUVs to improve their efficient sensing and maneuvering abilities.

REFERENCES

[1] J. M. Fulford, "Accuracy and consistency of water-current meters," *J. Amer. Water Resour. Assoc.*, vol. 37, no. 5, pp. 1215–1224, Oct. 2001.

[2] H. Bleckmann, J. Mogdans, and S. L. Coombs, *Flow Sensing in Air and Water*, 1st ed. Berlin, Germany: Springer, 2014.

[3] J. Kitzhofer, T. Nonn, and C. Brücker, "Generation and visualization of volumetric PIV data fields," *Experim. Fluids*, vol. 51, no. 6, pp. 1471–1492, Dec. 2011.

[4] G. Xiao, B. Wang, Z. Deng, M. Fu, and Y. Ling, "An acoustic communication time delays compensation approach for master–slave AUV cooperative navigation," *IEEE Sensors J.*, vol. 17, no. 2, pp. 504–513, Jan. 2017.

[5] G. Liu, S. Gao, T. Sarkodie-Gyan, and Z. Li, "A novel biomimetic sensor system for vibration source perception of autonomous underwater vehicles based on artificial lateral lines," *Meas. Sci. Technol.*, vol. 29, no. 12, Dec. 2018, Art. no. 125102.

[6] W. J. Van Trump and M. J. McHenry, "The morphology and mechanical sensitivity of lateral line receptors in zebrafish larvae (Danio rerio)," *J. Experim. Biol.*, vol. 211, no. 13, pp. 2105–2115, Jul. 2008.

[7] K. Pohlmann, J. Atema, and T. Breithaupt, "The importance of the lateral line in nocturnal predation of piscivorous catfish," *J. Experim. Biol.*, vol. 207, no. 17, pp. 2971–2978, Aug. 2004.

[8] S. Coombs and C. B. Braun, "Information processing by the lateral line system," in *Sensory Processing in Aquatic Environments*, S. P. Collin and N. J. Marshall, Eds. New York, NY, USA: Springer, 2003, pp. 122–138.

[9] G. Liu, "Research on flow field perception based on artificial lateral line sensor system," *Sensors*, vol. 18, no. 3, pp. 838–862, Mar. 2018.

[10] L. DeVries, F. D. Lagor, H. Lei, X. Tan, and D. A. Paley, "Distributed flow estimation and closed-loop control of an underwater vehicle with a multimodal artificial lateral line," *Bioinspiration Biomimetics*, vol. 10, no. 2, Mar. 2015, Art. no. 025002.

[11] T. Shizhe, "Underwater artificial lateral line flow sensors," *Microsyst. Technol.*, vol. 20, no. 12, pp. 2123–2136, 2014.

[12] M. N. M. Nawi, A. A. Manaf, M. R. Arshad, and O. Sidek, "Review of MEMS flow sensors based on artificial hair cell sensor," *Microsyst. Technol.*, vol. 17, no. 9, pp. 1417–1426, Sep. 2011.

[13] J. Chen, Z. Fan, J. Zou, J. Engel, and C. Liu, "Two-dimensional micromachined flow sensor array for fluid mechanics studies," *J. Aerosp. Eng.*, vol. 16, no. 2, pp. 85–97, Apr. 2003.

[14] Y. Yang, N. Chen, C. Tucker, J. Engel, S. Pandya, and C. Liu, "From artificial hair cell sensor to artificial lateral line system: Development and application," in *Proc. IEEE 20th Int. Conf. Micro Electro Mech. Syst. (MEMS)*, Jan. 2007, pp. 577–580.

[15] Y. Yang, A. Klein, H. Bleckmann, and C. Liu, "Artificial lateral line canal for hydrodynamic detection," *Appl. Phys. Lett.*, vol. 99, no. 2, Jul. 2011, Art. no. 023701.

[16] M. J. McHenry, J. A. Strother, and S. M. van Netten, "Mechanical filtering by the boundary layer and fluid–structure interaction in the superficial neuromast of the fish lateral line system," *J. Comparative Physiol. A*, vol. 194, no. 9, pp. 795–810, Sep. 2008.
[17] S. Peleshanko, M. D. Julian, M. Ornatska, M. E. McConney, M. C. LeMieux, N. Chen, C. Tucker, Y. Yang, C. Liu, J. A. C. Humphrey, and V. V. Tsukruk, "Hydrogel-encapsulated microfabricated haircells mimicking fish cupula neuromast," *Adv. Mater.*, vol. 19, no. 19, pp. 2903–2909, Oct. 2007.
[18] N. Izadi and J. M. K. Gijs, "Design and fabrication process for artificial lateral line sensors," in *Frontiers in Sensing From Biology to Engineering the Lateral Line*, S. Coombs, Ed. New York, NY, USA: Springer, 2012, pp. 405–419.
[19] N. Izadi, M. J. de Boer, J. W. Berenschot, and G. J. M. Krijnen, "Fabrication of superficial neuromast inspired capacitive flow sensors," *J. Micromech. Microeng.*, vol. 20, no. 8, Aug. 2010, Art. no. 085041.
[20] G. Krijnen, T. Lammerink, R. Wiegerink, and J. Casas, "Cricket inspired flow-sensor arrays," in *Proc. IEEE Sensors*, Oct. 2007, pp. 539–546.
[21] J. B. Stocking, W. C. Eberhardt, Y. A. Shakhsheer, B. H. Calhoun, J. R. PAULUS, and M. Appleby, "A capacitance-based whisker-like artificial sensor for fluid motion sensing," in *Proc. IEEE Sensors*, Nov. 2010, pp. 2224–2229.
[22] M. Asadnia, A. G. P. Kottapalli, Z. Shen, J. Miao, and M. Triantafyllou, "Flexible and surface-mountable piezoelectric sensor arrays for underwater sensing in marine vehicles," *IEEE Sensors J.*, vol. 13, no. 10, pp. 3918–3925, Oct. 2013.
[23] A. T. Abdulsadda and X. Tan, "Underwater source localization using an IPMC-based artificial lateral line," in *Proc. IEEE Int. Conf. Robot. Autom.*, May 2011, pp. 447–452.
[24] A. T. Abdulsadda and X. Tan, "An artificial lateral line system using IPMC sensor arrays," *Int. J. Smart Nano Mater.*, vol. 3, no. 3, pp. 226–242, Sep. 2012.
[25] F. Li, W. Liu, C. Stefanini, X. Fu, and P. Dario, "A novel bioinspired PVDF micro/nano hair receptor for a robot sensing system," *Sensors*, vol. 10, no. 1, pp. 994–1011, 2010.
[26] X. Yu, J. Tao, and J. Berilla, "A bio-inspired flow sensor," *Proc. SPIE*, vol. 7646, Mar. 2010, Art. no. 764618.
[27] J. Tao, X. Yu, and J. Berilla, "Micropillar sensing element for bioInspired flow sensors," in *Proc. 8th Int. Workshop Struct. Health Monitor.*, Standford, CA, USA, 2011, pp. 1732–1741.
[28] J. Tao, X. Yu, and J. Berilla, "Bio-inspired flow and acoustic sensor," *Proc. SPIE*, vol. 8019, Apr. 2011, Art. no. 80190R.
[29] X. M. Jing, J. M. Miao, T. Xu, and L. Norford, "Hair-like airflow sensing with piezoelectric vibrating diaphragm," in *Proc. IEEE Sensors*, Nov. 2010, pp. 1809–1812.
[30] X. M. Jing, J. M. Miao, T. Xu, M. Olfatnia, and L. Norford, "Vibration characteristics of micromachined piezoelectric diaphragms with a standing beam subjected to airflow," *Sens. Actuators A, Phys.*, vol. 164, nos. 1–2, pp. 22–27, Nov. 2010.
[31] A. Klein and H. Bleckmann, "Determination of object position, vortex shedding frequency and flow velocity using artificial lateral line canals," *Beilstein J. Nanotechnol.*, vol. 2, pp. 276–283, Jun. 2011.
[32] S. Große and W. Schröder, "The micro-pillar shear-stress sensor MPS_3 for turbulent flow," *Sensors*, vol. 9, no. 4, pp. 2222–2251, Mar. 2009, doi: 10.3390/s90402222.
[33] V. I. Fernandez, S. M. Hou, F. S. Hover, J. H. Lang, and M. S. Triantafyllou, *Lateral-Line Inspired MEMS Array Pressure Sensing for Passive Underwater Navigation Technical Report*. MIT, Cambridge, MA, USA, 2007.
[34] F. M. Yaul, V. Bulovic, and J. H. Lang, "A flexible underwater pressure sensor array using a conductive elastomer strain gauge," *J. Microelectromech. Syst.*, vol. 21, no. 4, pp. 897–907, Aug. 2012.
[35] J. E. Dusek, M. S. Triantafyllou, and J. H. Lang, "Piezoresistive foam sensor arrays for marine applications," *Sens. Actuators A, Phys.*, vol. 248, pp. 173–183, Sep. 2016.
[36] H. Herzog, A. Klein, H. Bleckmann, P. Holik, S. Schmitz, G. Siebke, S. Tätzner, M. Lacher, and S. Steltenkamp, "μ-biomimetic flow-sensors—Introducing light-guiding PDMS structures into MEMS," *Bioinspiration Biomimetics*, vol. 10, no. 3, Apr. 2015, Art. no. 036001.
[37] Y. Jiang, Z. Ma, J. Fu, and D. Zhang, "Development of a flexible artificial lateral line canal system for hydrodynamic pressure detection," *Sensors*, vol. 17, no. 6, pp. 1220–1230, 2017.
[38] V. Nguyen, S. Melkote, A. Deshamudre, M. Khanna, and D. Walker, "PVDF sensor based monitoring of single-point cutting," *J. Manuf. Processes*, vol. 24, pp. 328–337, Oct. 2016.
[39] L. Qi, J. Xing, D. Shang, and Y. Wang, "A flow velocity measurement method based on a PVDF piezoelectric sensor," *Sensors*, vol. 19, no. 7, pp. 1657–1670, Apr. 2019, doi: 10.3390/s19071657.
[40] F. Liu, N. A. Hashim, Y. Liu, M. R. M. Abed, and K. Li, "Progress in the production and modification of PVDF membranes," *J. Membrane Sci.*, vol. 375, nos. 1–2, pp. 1–27, Jun. 2011.
[41] *LDT0-028K Piezo Vibration Rev 1*. Accessed: 2021. [Online]. Available: www.meas-spec.com
[42] J. Park, K. Kwon, and H. Choi, "Numerical solutions of flow past a circular cylinder at Reynolds numbers up to 160," *J. Mech. Sci. Technol.*, vol. 12, no. 6, pp. 1200–1205, 1998.
[43] B. G. Dehkordi and H. H. Jafari, "Numerical simulation of flow through tube bundles in in-line square and general staggered arrangements," *Int. J. Numer. Methods Heat Fluid Flow*, vol. 19, no. 8, pp. 1038–1062, Sep. 2009.
[44] M. M. Rahman, M. M. Karim, and M. A. Alim, "Numerical investigation of unsteady flow past a circular cylinder using 2-D finite volume method," *J. Nav. Archit. Mar. Eng.*, vol. 4, no. 1, pp. 27–42, Jan. 1970.
[45] R. M. Stringer, J. Zang, and A. J. Hillis, "Unsteady RANS computations of flow around a circular cylinder for a wide range of Reynolds numbers," *Ocean Eng.*, vol. 87, pp. 1–9, Sep. 2014.
[46] *Academic Research, Release 13.0, Help System, CFX Reference Guide, 6.3.4.1.5.2: Integration to the Wall (Low-Reynolds Number Formulaton)*, ANSYSs, Canonsburg, PA, USA, 2010.
[47] A. C. Benim, M. Cagan, A. Nahavandi, and E. Pasqualotto, "RANS predictions of turbulent flow past a circular cylinder over the critical regime," in *Proc. 5th Iasme/Wseas Int. Conf. Fluid Mech. Aerodyn. (FMA)*, 2007, pp. 235–240.
[48] H. Lei, W. Li, and X. Tan, "Encapsulation of ionic polymer-metal composite (IPMC) sensors with thick parylene: Fabrication process and characterization results," *Sens. Actuators A, Phys.*, vol. 217, pp. 1–12, Sep. 2014.
[49] X. Zhang, X. Shan, Z. Shen, T. Xie, and J. Miao, "A new self-powered sensor using the radial field piezoelectric diaphragm in d33 mode for detecting underwater disturbances," *Sensors*, vol. 19, no. 4, pp. 962–976, 2019.
[50] M. Asadnia, A. G. P. Kottapalli, Z. Shen, J. Miao, and M. Triantafyllou, "Artificial fish skin of self-powered micro-electromechanical systems haircells for sensing hydrodynamic flow phenomena," *J. R. Soc. Interface*, vol. 10, no. 83, pp. 1–14, 2015.
[51] A. Dagamseh, R. Wiegerink, T. Lammerink, and G. Krijnen, "Imaging dipole flow sources using an artificial lateral-line system made of biomimetic hair flow sensors," *J. R. Soc. Interface*, vol. 12, no. 83, pp. 1–9, 2015.
[52] J. Goulet, J. Engelmann, B. P. Chagnaud, J.-M.-P. Franosch, M. D. Suttner, and J. L. van Hemmen, "Object localization through the lateral line system of fish: Theory and experiment," *J. Comparative Physiol. A*, vol. 194, no. 1, pp. 1–17, Jan. 2008.
[53] M. E. McConney, N. Chen, D. Lu, H. A. Hu, S. Coombs, C. Liu, and V. V. Tsukruk, "Biologically inspired design of hydrogel-capped hair sensors for enhanced underwater flow detection," *Soft Matter*, vol. 5, no. 2, pp. 292–295, 2009.
[54] M. Bora, A. G. P. Kottapalli, J. Miao, and M. S. Triantafyllou, "Biomimetic hydrogel-CNT network induced enhancement of fluid-structure interactions for ultrasensitive nanosensors," *NPG Asia Mater.*, vol. 9, p. 440, Oct. 2017.
[55] *FlowTracker2 Lab ADV: SNR, Sampling Rate and Velocity Range Effects on data, Technical Paper*. Accessed: 2021. [Online]. Available: http://www.sontex.com
[56] H. Herzog, J. Mogdans, and H. Bleckmann, "Smart mechanical dipole: A device for the measurement of sphere motion in behavioral and neurophysiological experiments," *J. Experim. Biol.*, vol. 219, no. 18, pp. 2823–2827, Sep. 2016.
[57] Z. Tang, Z. Wang, J. Lu, G. Ma, and P. Zhang, "Underwater robot detection system based on fish's lateral line," *Electronics*, vol. 8, no. 5, pp. 1–12, 2019.
[58] M. Krieg, K. Nelson, and K. Mohseni, "Distributed sensing for fluid disturbance compensation and motion control of intelligent robots," *Nature Mach. Intell.*, vol. 1, no. 5, pp. 216–224, May 2019.
[59] B. J. Wolf, S. Warmelink, and S. M. van Netten, "Recurrent neural networks for hydrodynamic imaging using a 2D-sensitive artificial lateral line," *Bioinspiration Biomimetics*, vol. 14, no. 5, Sep. 2019, Art. no. 055001.

[60] B. J. Wolf and S. M. van Netten, "Hydrodynamic imaging using an all-optical 2D Artificial lateral line," in *Proc. IEEE Sensors Appl. Symp. (SAS)*, Mar. 2019, pp. 1–6.
[61] L. DeVries, F. D. Lagor, H. Lei, X. Tan, and D. A. Paley, "Distributed flow estimation and closed-loop control of an underwater vehicle with a multi-modal artificial lateral line," *Bioinspiration Biomimetics*, vol. 10, no. 2, Mar. 2015, Art. no. 025002.
[62] Y. Jiang, Z. Ma, and D. Zhang, "Flow field perception based on the fish lateral line system," *Bioinspiration Biomimetics*, vol. 14, no. 4, pp. 1–24, 2019.
[63] M. S. Triantafyllou, G. D. Weymouth, and J. Miao, "Biomimetic survival hydrodynamics and flow sensing," *Annu. Rev. Fluid Mech.*, vol. 48, no. 1, pp. 1–24, Jan. 2016.
[64] V. I. Fernandez, A. Maertens, F. M. Yaul, J. Dahl, J. H. Lang, and M. S. Triantafyllou, "Lateral-line-inspired sensor arrays for navigation and object identification," *Mar. Technol. Soc. J.*, vol. 45, no. 4, pp. 130–146, Jul. 2011.
[65] S. Lakkam, B. T. Balamurali, and R. Bouffanais, "Hydrodynamic object identification with artificial neural models," *Sci. Rep.*, vol. 9, no. 1, pp. 1–12, Dec. 2019.

TAN SHIZHE was born in Shandong, China, in 1971. He received the B.S. and M.S. degrees in mechanical and electronic engineering from Shandong University, Shandong, in 1993 and 1996, respectively, and the Ph.D. degree in mechanical engineering from Shanghai Jiao Tong University, Shanghai, in 2002.

From 2002 to 2005, he was engaged in post-doctoral research at the Robot Laboratory, Harbin Institute of Technology. Since 2005, he has been an Assistant Professor with the Electronic Engineering Department, Ocean University of China. He is the author of several books and more than 20 articles, and holds five invention patents. His research interests include underwater sensors and applications.

Mr. Shizhe's awards and honors include the First Prize of the Science and Technology Progress Award of the China Navigation and Positioning Association.

WANG YIJIN was born in Shanxi, China, in 1998. She received the B.S. degree in electronic information engineering from the Shandong University of Science and Technology, Qingdao, China, in 2020. She is currently pursuing the M.S. degree in communication and information systems with the Ocean University of China.

From 2020 to 2021, she was working on artificial lateral line sensors. Her current research interest includes the design and calibration of artificial lateral line sensor based on PVDF and the location of dipole resources.